Development of a Self-Aligned Compact Focusing Schlieren System for NASA Test Facilities

Brett F. Bathel[*] and Joshua M. Weisberger[†]

NASA Langley Research Center, Hampton, Virginia, 23681

A novel compact, inherently self-aligned focusing schlieren system is presented for use in experiments that require flow visualization. Unlike existing focusing schlieren systems that require a separate, and precisely aligned, source grid and cutoff grid to achieve sensitivity to density gradients, this system projects an image of a physical grid element onto a background and then reimages this projection back onto the physical grid element thereby achieving self-alignment. Further, unlike existing focusing schlieren systems where the image of the source grid is physically translated relative to the cutoff grid to achieve sensitivity to density gradients, a polarization prism in the system acts on the polarization state of the light of the projected grid element to provide sensitivity adjustment. By adjusting the position of the prism along the optical axis of the instrument, changes to the sensitivity can be realized. Since the outgoing and returning light used to project an image of the grid element are orthogonally polarized to one another, reflections from windows that may be present between the lens and background of the system can be eliminated. The system can also be implemented in test facilities where optical access is limited and/or exists on only one side. A discussion on different aspects of the development of this technology is provided, as are sample images from the system at the different stages of development. Images that demonstrate the ability to make on-the-fly adjustments to the instrument's field-of-view and working distance are also presented.

I. Nomenclature

$C_{source/cutoff}$	=	source/cutoff grid spatial frequency [lp/mm]
CD	=	condenser/diffuser lens
D_{jet}	=	jet nozzle diameter [mm]
F_S	=	imaging acquisition rate [Hz]
f_{lens}	=	primary lens focal length [mm]
h_{Rochon}	=	Rochon prism face height [mm]
I	=	transmitted intensity [A.U.]
I_0	=	initial intensity [A.U.]
LP	=	linear polarizer
lcp	=	left circularly polarized
lhp	=	linear horizontally polarized
lvp	=	linear vertically polarized
RBG	=	retroreflective background
rcp	=	right circularly polarized
QWF	=	quarter-wave film
QWP	=	quarter-wave plate
t_{Rochon}	=	Rochon prism thickness [mm]
w_{Rochon}	=	Rochon prism face width [mm]
$\tilde{z}_{cutoff}$	=	cutoff grid location relative to primary lens [mm]
$\tilde{z}_{density}$	=	density object location relative to primary lens [mm]
$\tilde{z}_{RBG}$	=	background location relative to primary lens [mm]
$\tilde{z}_{Rochon}$	=	Rochon prism spacing relative to grid element [mm]
$\tilde{z}_{sensor}$	=	sensor plane location relative to primary lens [mm]

*Research Engineer, Advanced Measurements and Data Systems Branch, MS 63, AIAA Senior Member.
†Research Engineer, Advanced Measurements and Data Systems Branch, MS 63, AIAA Member.

α	=	Rochon prism interface angle [°]
β	=	Rochon prism exit beam angle [°]
δ_{cutoff}	=	cutoff grid translation adjustment [mm]
$\%_{\text{cutoff}}$	=	percentage cutoff

II. Introduction

Focusing schlieren is a useful flow visualization technique that allows for imaging of density gradients over a plane with a narrow depth-of-focus (DOF). The narrow DOF of the focusing schlieren system allows the user to filter out unwanted features that might otherwise contribute to noise in the final schlieren image which is common to path-integrated schlieren-based techniques such as conventional schlieren (including Toepler's single lens system[1], dual parabolic mirror z-type systems, and dual lens systems), background-oriented schlieren (BOS), and shadowgraph. Another benefit of focusing schlieren is that, like BOS and shadowgraph methods, the field-of-view (FOV) is not limited to the clear aperture of the optics used in the system, which is a limitation of conventional schlieren systems. Focusing schlieren also does not require the use of so-called 'schlieren-grade' windows to obtain high-quality images as is the case with conventional schlieren and some BOS and shadowgraph setups. A comprehensive review of these path-integrated schlieren-based methods, and the focusing schlieren method, is provided in the book by Settles [2]. More recent developments to the methods are reviewed in Ref. [3].

Modern focusing schlieren systems can be classified into five major types that are presented in Fig. 1 that descend from the original focusing schlieren systems developed in the 1940s by Hartmann [4, 5] and later by Schardin [6] and Burton [7]. The first, and most common, is the conventional modern focusing schlieren system perfected by Weinstein [8, 9] shown schematically in Fig. 1a. Here, light from an illumination source is passed through a Fresnel lens located directly behind a source grid that loosely focuses the light into a lens on the opposite side of the measurement volume. The use of the Fresnel lens was originally recommended by Boedeker [10] to improve brightness. The source grid in this setup typically consists of a regular pattern of transparent and opaque lines with a spatial frequency of C_{source} given in line pairs per mm (lp/mm). It should be placed at least 25 mm from the Fresnel lens to minimize artifacts in the final schlieren image resulting from the concentric elements of the Fresnel lens as recommended by Weinsten [8]. The lens serves to image the source grid onto a cutoff grid, which is an exact scaled copy of the source grid with a spatial frequency of C_{cutoff}. The placement of the source grid and cutoff grid along the instrument's optical axis relative to the lens is approximately determined by application of the thin lens equation. By translating the cutoff grid by a small distance, $0 \leq \delta_{\text{cutoff}} \leq 1/(2 \cdot C_{\text{cutoff}})$, in a direction orthogonal to the instrument's optical axis and to the lines on the grid, varying degrees of sensitivity to density gradients in the plane of the density object can achieved. The extent of δ_{cutoff} beyond which no additional gain in sensitivity is achieved corresponds to the width of a transparent line on the cutoff grid. Focusing schlieren images are acquired at the image plane whose approximate position along the instrument's optical axis is determined relative to the density object plane and lens location via the thin lens equation. The focusing schlieren method of operation is similar in nature to a conventional schlieren system where a single knife edge is adjusted to vary the sensitivity of the instrument. With the focusing schlieren system, however, the transparent lines of the source grid are akin to multiple independent schlieren light sources while the opaque lines on the cutoff grid are akin to multiple independent schlieren knife edges. The narrow DOF of the system comes from: (1) the superposition of schlieren images from the independent sources on the source grid amplifying the common signal among them – corresponding to the density object plane – while averaging out the uncommon signals and (2) the imaging properties of the lens as noted by Boedeker [10]. Examples of the conventional modern focusing schlieren system applied in ground test facilities at the NASA Langley Research Center can be found in Refs. [11, 12].

In 1996, Heineck [13] proposed a variant of the modern focusing schlieren system that moved all components but the source grid to one side of the measurement volume as shown in Fig. 1b. In this configuration, a retroreflective background is covered with an opaque grid pattern. Light from an illumination source on the camera side of the instrument is coupled onto the optical axis via a beamsplitter. Upon reflection from the background, the light returns to the instrument with a portion transmitted by the beamsplitter into the imaging lens, through the cutoff grid, and onto the image plane. The benefit of this arrangement is that the retroreflective source grid can easily be mounted to the interior of a wind tunnel wall, eliminating the need for optical access on two sides of the measurement volume. The retroreflective material also provides an efficient method of coupling light into the imaging lens without the artifacts from concentric lens elements in a Fresnel lens. As with the conventional modern focusing schlieren system, the placement of the source grid, imaging lens, cutoff grid, and imaging plane are dictated by the thin lens equation and sensitivity is again adjusted by translating the cutoff grid by some distance δ_{cutoff}.

A similar approach to [13] was developed by Weinstein [14] and Fagan *et al.* [15], but with a projected source grid pattern originating from a source grid element on the camera-side of the instrument which is displayed on a retroreflective background. This method is shown in Fig. 1c. Like [13], the projection axis is made collinear with the imaging axis by way of a beamsplitter. The projected source grid is then imaged by a pair of lenses onto a cutoff grid, and an imaging camera is used to capture focusing schlieren images. As with Heineck's method, the use of a retroreflective background eliminates the need for optical access on two sides of the measurement volume and is free of artifacts that would otherwise be present in a Fresnel lens.

Recently developed digital focusing schlieren instruments described in Refs. [16–19], shown in Figs. 1d and 1e, make it possible to significantly reduced the time required to align the source and cutoff grid elements to one another. In Fig. 1d, a back-illuminated digital screen displays a computer-generated source grid pattern that is aligned to the cutoff grid on the camera-side of the instrument. In Fig. 1e, a digital projector is instead used to project a computer-generated source grid pattern onto the background. Unlike the other focusing schlieren methods shown in Fig. 1 where the cutoff grid is fabricated to match the source grid, these systems optimize the displayed source grid to match the cutoff grid. While the back-illuminated version in Fig. 1d is limited to low-speed applications because of the limited intensity output of back-illuminated digital displays, more recent work [20] has shown that transparent digital displays back-illuminated by a pulsed laser source can accommodate higher-speed (>1 kHz) imaging applications. The projector-based version in Fig. 1e has the additional benefit of working in facilities with optical access only on one side of the measurement volume.
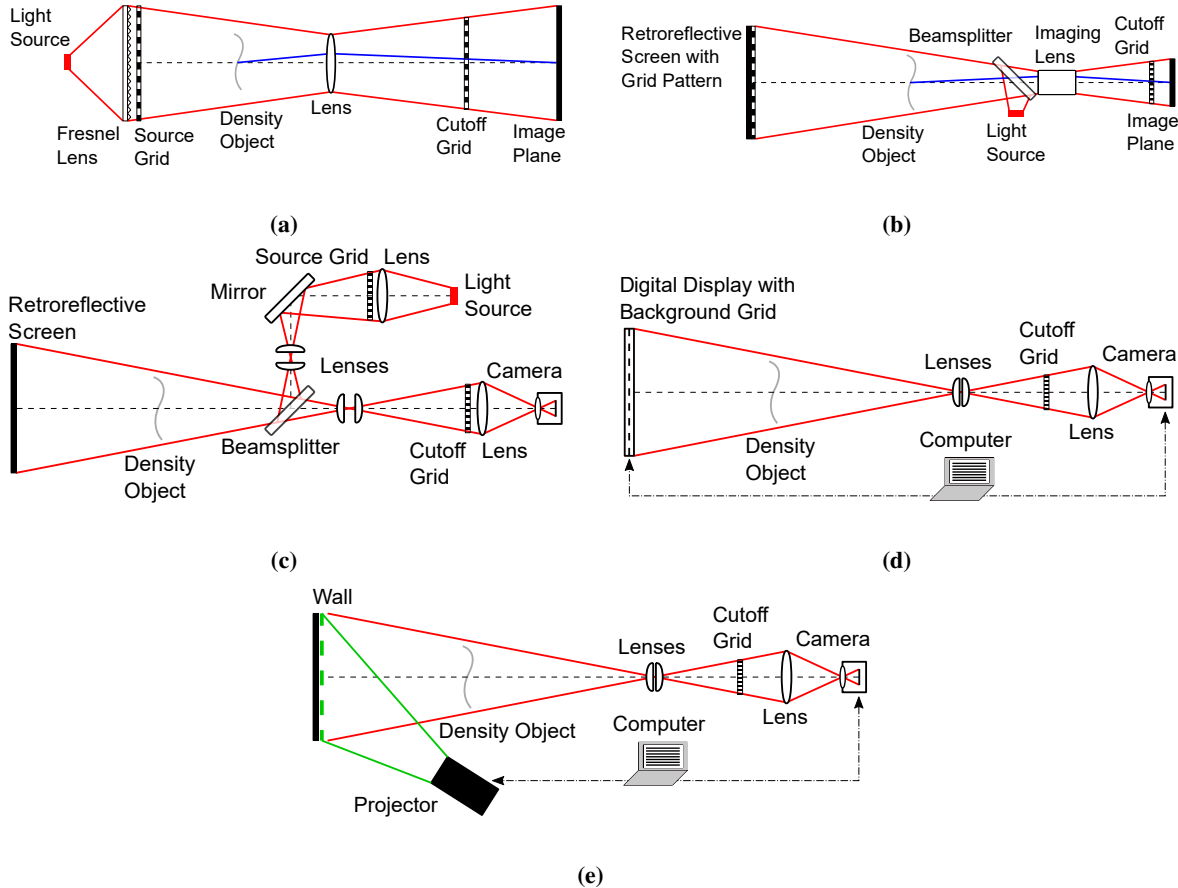

Fig. 1   Five major types of focusing schlieren systems including (a) conventional modern focusing schlieren [8, 9], (b) retroreflection focusing schlieren [13], (c) projection focusing schlieren [14, 15], (d) digital and (e) digital projection focusing schlieren [16–19]. Images adapted from listed references.

Recent work on visualization of plume/surface interactions (PSI) at NASA Langley Research Center motivated the need to identify a high-speed focusing schlieren imaging technique that could provide visualization of the PSI gas

flowfield. While path-averaged BOS and shadowgraph techniques were also considered for this work, there was a desire to filter out the noise from flow structures and ejecta particles away from the measurement plane of interest. The following is a list of all of the qualities that were required of the system to ensure success during the measurement campaigns:

1) Ability to filter out signal from flow structures and Martian/lunar regolith simulant ejecta particles away from the measurement plane of interest
2) Relatively high sensitivity to density gradients from the nozzle plume gas in a low density, near-vacuum environment
3) A system that was relatively simple and quick to align, and would remain aligned when the facility was brought to a near-vacuum condition
4) A compact instrument that could fit within a relatively small environmental enclosure when operated in the near-vacuum environment
5) A system where the source grid hardware fit within a limited footprint and could survive in the near-vacuum environment
6) A system capable of high-speed acquisition rates F_S (20 kHz$\leq F_S \leq$100 kHz)
7) A system that was insensitive to relatively intense facility vibrations
8) A system where changes to the working distance and FOV could be adjusted with relative ease, and one where relatively large FOVs (> 100 mm) could be achieved, without major modification to the optical layout of the system

While all of the aforementioned focusing schlieren systems presented in Fig. 1 satisfied items 1 and 2 in the list above, no system was able to satisfy the remaining 6 items satisfactorily. While the digital systems shown in Figs. 1d and 1e are highly versatile, their use was ruled out as: 1) misalignment between the digital source grid and cutoff grid from facility vibrations would affect image quality, 2) the digital display elements would not provide sufficient signal for the high-speed acquisition rates required, and 3) the footprint of the digital source grid hardware was too large and its ability to survive in a near-vacuum environment was unknown. The projection focusing schlieren system was ruled out as: 1) there was potential for misalignment between the separate source and cutoff grids, 2) the arrangement was not compact but rather heavy and bulky as noted in Ref. [18], and 3) glints from window reflections in an environmental enclosure could limit the image quality as noted in Ref. [14]. The retroreflection focusing schlieren system was ruled out as: 1) there was significant potential for misalignment of the source and cutoff grids and 2) it was likely that glints from window reflections in an environmental enclosure would occur. Finally, the conventional modern focusing schlieren system was ruled out as: 1) there was significant potential for misalignment of the source and cutoff grids and 2) the source grid hardware was not compact.

As a result, an effort to develop a compact focusing schlieren system that could meet the requirements outlined above was undertaken. Additionally, if this development effort was successful, the resulting system would have the potential to be of great benefit for other topics of research that utilize ground test facilities and flow visualization methods across all speed regimes. The purpose of this paper is to describe the development process for a novel, self-aligned compact focusing schlieren system for use in ground testing applications and discuss lessons learned during this process. The system operates in a fundamentally different way compared to existing focusing schlieren systems in that it acts on the polarization state of light to provide sensitivity adjustment and is inherently self-aligned. Additionally, the compact nature of the system allows for it to simply be mounted to the front of a camera similar to a conventional camera lens. A set of sample results is provided to show the data products that can be expected from this system.

III. Development of an Initial Self-Aligned Compact Focusing Schlieren System

A. Self-Alignment: Eliminating the Complexity of Separate Source and Cutoff Grids

While focusing schlieren is a very useful flow visualization technique, the biggest hurdle in its successful implementation is the alignment procedure, which requires the user to create a cutoff grid that is perfectly matched and scaled to an image of the source grid (or in the case of the digital methods, create a source grid that is perfectly matched and scaled to the cutoff grid). In all the methods presented in Fig. 1, two separate sub-systems are needed to create each grid. After considering these approaches, it became apparent that the best way to achieve a cutoff grid that was perfectly matched and scaled to a source grid was to use a lens to project an image of the cutoff grid onto some background, and

then use the same lens to image this projected grid back onto the original cutoff grid. The position of the cutoff grid, the lens, and the background onto which it is projected can be approximated by application of the thin lens equation:

$$\frac{1}{f_{\text{lens}}} \approx \frac{1}{\tilde{z}_{\text{RBG}}} + \frac{1}{\tilde{z}_{\text{cutoff}}} \tag{1}$$

where f_{lens} is the lens focal length in mm, $\tilde{z}_{\text{RBG}}$ is the spacing between the lens and the background, and $\tilde{z}_{\text{cutoff}}$ is the spacing between the lens and the cutoff grid. Using this approach, the need for a separate source grid could be eliminated, the overall complexity of the system reduced and most importantly, the system would become inherently self-aligned. As a result, the method of projecting a single grid element onto a background, and then imaging that projection back onto the same grid to achieve self-alignment, was chosen as the approach for development of our self-aligned compact focusing schlieren system.

B. Sensitivity Adjustment

The next challenge was to develop a way to adjust the sensitivity of the focusing schlieren system. In Figs. 1a, 1b, and 1c, the cutoff grid must be physically translated relative to the image of the source grid to adjust the instrument's sensitivity to density gradients at the density object plane. In Figs. 1d and 1e, the displayed computer-generated source grid that must be translated to adjust sensitivity. With the self-aligned concept, any physical translation of the grid element has no effect on sensitivity since the image of the projected grid element is simply imaged back onto the original grid element. Thus, an optic was needed to redirect only the light returning from the projected grid element such that the image it formed on the original grid element could be translated relative to that grid element.

One option that was considered was to use light of one wavelength to project an image of the grid element onto a background that itself would absorb that wavelength and then re-emit light at a different wavelength. An optic would then be used to act on this emitted wavelength such that the image of the projected grid on the original grid element could be translated and an adjustment in sensitivity realized. This option was quickly ruled out as it would have: 1) significantly added to the complexity of the system and 2) limited the acquisition rate of the instrument as the emission intensity from absorbing/emitting materials (e.g., a fluorescent sheet) would be relatively low. The other option was to use an optic to act on the polarization state of the light. Our previous work with the focusing laser differential interferometer (FLDI) led us to consider the use of polarizing prisms, such as the Wollaston and Nomarski prisms in Refs. [21, 22], to act on the returning (but not the outgoing) light. The Rochon prism was the first that seemed like the ideal prism needed to provide polarization-based sensitivity adjustment.

A schematic of an idealized Rochon prism is shown in Fig. 2a and provides details on how it acts on orthogonal components of linearly polarized light. Here, randomly polarized light (purple arrow) is incident on the entrance face of the prism. The orientation of the optical axes of the crystal structure in each half of the prism results in two orthogonally-polarized beams that exit the prism at an angle β relative to one another. Here, linear vertically polarized (*lvp*, red arrow) light exits the prism and is collinear with the randomly polarized incident beam while linear horizontally polarized (*lhp*, blue arrow) light exits the prism at an angle β relative to the *lvp* beam. Figure 2b shows the amount of translation imparted to the image of the projected grid at the plane of the grid element, which is approximately computed as:

$$\delta_{\text{cutoff}} \approx \left(\frac{t_{\text{Rochon}}}{2} + \tilde{z}_{\text{Rochon}} \right) \tan \beta \tag{2}$$

with the percentage of cutoff defined as:

$$\%_{\text{cutoff}} \approx 2\delta_{\text{cutoff}} C_{\text{cutoff}} \tag{3}$$

where t_{Rochon} is the Rochon prism thickness and $\tilde{z}_{\text{Rochon}}$ is the spacing between the exit face of the Rochon prism and the grid element plane. Figure 2c shows the initial quartz/quartz Rochon prism that was purchased from United Crystals® for the construction of this focusing schlieren system. The height (h_{Rochon}), width (w_{Rochon}), and thickness (t_{Rochon}) of the prism was 50 mm. The size of the prism was chosen to ensure a relatively large clear aperture for imaging tests and was compatible with typical 50.8-mm optics that were already available in the laboratory. The exit beam angle was selected to be $\beta \approx 0.5°$ (30 arc-minutes) so that a Ronchi ruling with a spatial frequency of $C_{\text{cutoff}} = 1$ lp/mm could be used as the grid element.

In an ideal Rochon prism, *lvp* light traveling in either direction through the prism (entrance-to-exit or exit-to-entrance) is unaffected by the prism, while *lhp* light is always refracted by a small angle β. This ideal behavior was precisely what was needed to provide a method of sensitivity adjustment in our system.
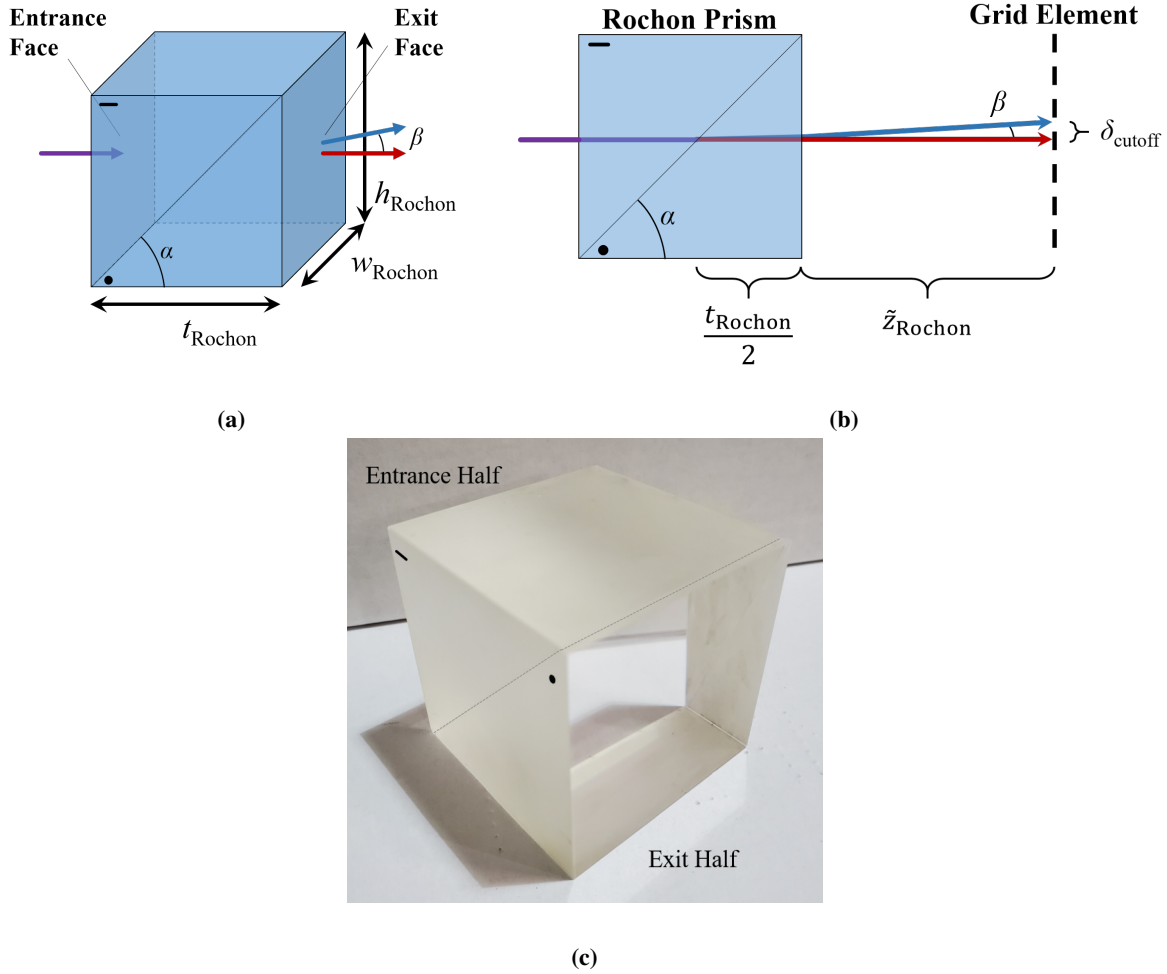
Fig. 2 **(a) Perspective view of the Rochon prism showing the general dimensions, prism interface angle α, and exit beam angle β. (b) Side view of Rochon prism and grid element showing relevant parameters used to compute δ_{cutoff}. The purple arrows indicate random polarization, the red arrows *lvp*, and the blue arrows *lhp*. (c) Image of initial Rochon prism purchased for construction of the focusing schlieren instrument, with optic axes of entrance and exit halves noted.**

C. Using Retroreflective Sheeting to Rotate the Polarization State

Although an optic had been identified that could impart a small shift δ_{cutoff} between the reimaged projection of the cutoff grid and the cutoff grid itself, a method was needed to rotate the polarization state of the light returning from the projected grid element on the background by 90° relative to the outgoing light. Initially, it was thought that a Faraday rotator could be used to perform this rotation task. This was quickly ruled out, however, as the clear apertures of commercially available Faraday rotators were small (< 5 mm) and therefore not appropriate for this imaging application. The next thought was to incorporate a simple optical isolator using only a polarizing beamsplitter (PBS), a mirror, and a quarter-wave plate (QWP) into the focusing schlieren system. In this simple optical isolator, *lhp* laser light is transmitted directly through a PBS and then passed through a QWP that alters the polarization state of light such that it is changed from being *lhp* to left circularly polarized (*lcp*). Upon reflection from the mirror, the handedness of the light is then switched from *lcp* to right circularly polarized (*rcp*). As this *rcp* light passes through the QWP a second time in the reverse direction, its polarization state is altered a final time from being *rcp* to being *lvp*. This light is then reflected out of the system by the PBS.

For the focusing schlieren system, the reverse of this simple optical isolator was considered. The thinking was that light from an illumination source could be made into *lvp* light by way of a linear polarizer (LP) and then reflected onto

the instrument's optical axis by way of a PBS. This *lvp* light would then back-illuminate the cutoff grid element and pass through the Rochon prism unrefracted. After passing through an appropriately oriented QWP, the light would be converted to *rcp* light and then passed through an imaging lens. This imaging lens would form an image of the cutoff grid element on a mirror-like background with the *rcp* light. Upon reflection from the mirror-like background surface, the *rcp* light would be converted to *lcp*. After passing through the imaging lens a second time, the *lcp* light would pass through the QWP and be converted to *lhp* light. As the returning *lhp* light then passed through the Rochon prism, it would be refracted by a small angle β relative to the outgoing *lvp* light. This refracted *lhp* light would then form an image of the projected cutoff grid onto the original cutoff grid element, which would act as a spatial filter similar to the knife edge in a conventional schlieren imaging system. This spatially-filtered *lhp* light would then pass through the PBS where an LP would provide additional polarization filtering to ensure strictly *lhp* light was allowed to pass on to the camera sensor.

The problem with this approach was that a satisfactory replacement for a silvered (or similar) mirror – typical of an optical isolator – needed to be identified, as a flat mirrored surface would reflect the outgoing diverging *rcp* light away from the instrument. The use of parabolic or spherical mirrors were first considered, as they could direct the reflected light directly back to the instrument. However, commercially available parabolic and spherical mirrors are typically limited in their size, with larger mirrors (≥ 1 m diameter) being relatively expensive. Since we had extensive experience using retroreflective sheeting for BOS and shadowgraph testing, and because a retroreflective screen had been successfully used with the projection focusing schlieren system shown in Fig. 1c, retroreflective sheeting was first attempted as the background material in our system. However, it was not known if the retroreflective sheeting would act on the polarization state of the incident light in a manner similar to a mirror.

A literature search found that very little work had been performed on the characterization of the polarization properties of retroreflective sheeting. Only one reference was identified that provided some information on the degree to which several brands of retroreflective sheeting could maintain the linear polarization state of light upon retroreflection [23]. In that paper, the test considered the maintenance of a single linear polarization state of light after reflection over a range of sheet tilt and rotation angles. No publication was found concerning the ability of retroreflective sheeting to reverse the handedness of circularly polarized light upon retroreflection. As a result, two tests were performed to characterize the polarization properties of the 3M™ Scotchlite™ 7610 High Gain Reflective Sheeting that would first be used with the system.

The first test was designed to characterize the polarization maintenance of the sheeting, with the test setup shown in Fig. 3a. Here, light from a 50 W white LED was passed through a 50-mm-diameter condenser/diffuser lens and an LP mounted in a rotation stage. The initially *lvp* light was then used to back illuminate a 1951 USAF calibration target. The image of the calibration target was then passed through a non-polarizing 50:50 beamsplitter plate angled at 45° relative to the optical axis and projected onto a piece of the retroreflective sheeting. The same lens and non-polarizing 50:50 beamsplitter plate were then used to image the projection of the calibration target onto a CMOS camera sensor fitted with an LP oriented such that it transmitted only *lvp* light. Figure 3b shows the image obtained with the CMOS camera, with the region used for analysis of the polarization maintenance highlighted by the yellow rectangle. For this test, the first/primary LP was rotated in 10° increments and the mean intensity, I, from the analysis region recorded. Figure 3c shows these measured mean intensities as a function of LP angle, θ_{LP}, with 0° and 180° corresponding to the transmission axis of both LPs being aligned to transmit *lvp* light. As θ_{LP} is increased, I begins to diminish until it essentially vanishes at $\theta_{\mathrm{LP}} = 90°$ when the transmission axes of the two LPs are orthogonal to one another. As the primary LP is rotated beyond this point, I begins to increase until the transmission axes of the two LPs are once again aligned at $\theta_{\mathrm{LP}} = 180°$. The fit of the I data in Fig. 3c, denoted by the red curve, follows the Law of Malus [24] that describes the transmitted intensity of light through two LPs relative to the initial intensity, I_0, as one LP is rotated relative to the other:

$$I = I_0 \cdot \cos^2(\theta_{\mathrm{LP}}) \tag{4}$$

The results of this test showed that the retroreflective sheeting maintained the state of incident linear polarization for all linear polarization angles.

The next test was designed to characterize the ability of the retroreflective sheeting to reverse the handedness of circular polarization upon retroreflection. This test required only a few modifications to the setup shown in Fig. 3a with the full setup shown in Fig. 4a. For this test, the angle of the primary LP was fixed such that it only transmitted *lhp* light, a PBS replaced the non-polarizing 50:50 beamsplitter plate, a $C_{\mathrm{cutoff}} = 1$ lp/mm Ronchi ruling replaced the 1951 USAF calibration target, a QWP on a rotation mount was placed between the lens and the PBS, and the secondary LP on the CMOS camera was oriented such that it only passed *lvp* light. In this setup, the PBS transmits *lhp* light and reflects *lvp*
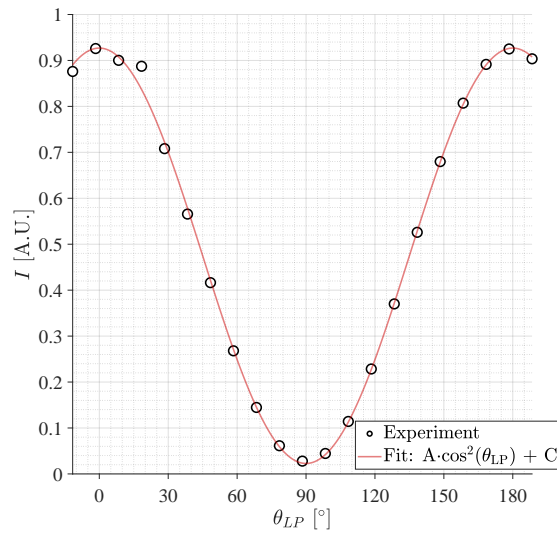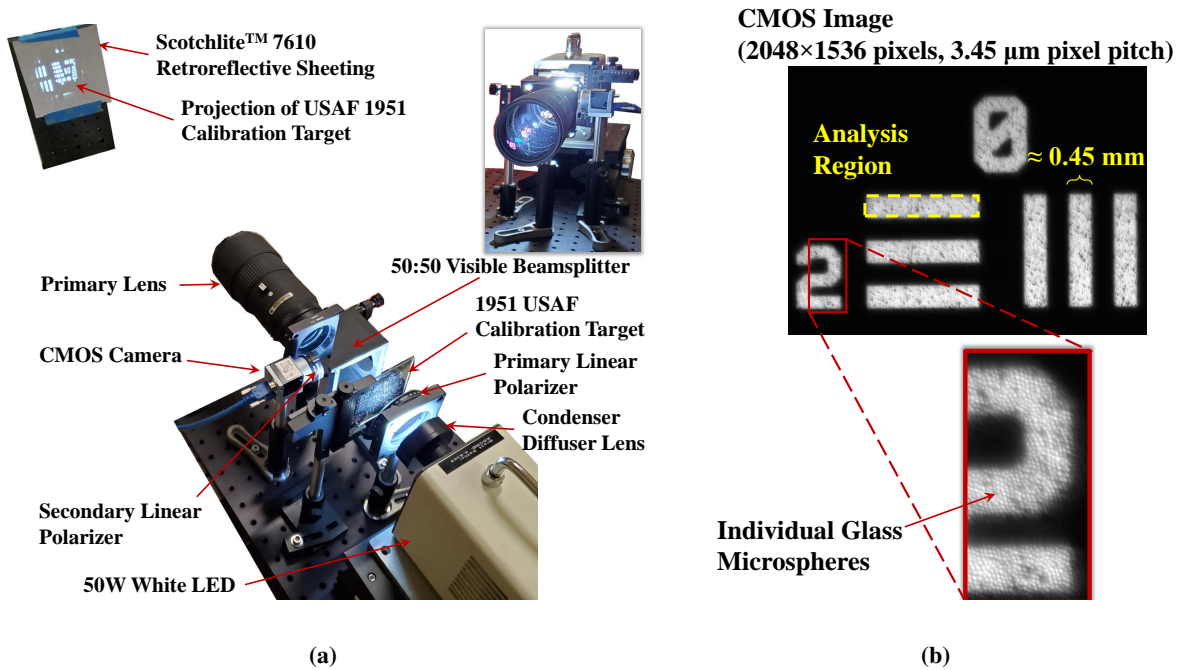
(a)

(b)

(c)

Fig. 3 **(a) Experimental setup used to characterize the ability of the retroreflective sheeting to maintain linear polarization. (b) Image of group 0, element 2 on the projected 1951 USAF calibration target imaged by the CMOS camera. (c) Intensity variation measurements as a function of primary LP angle, θ_{LP}.**

light. An image of the projected Ronchi ruling is shown in Fig. 4b. Similar to the first test, the mean of I from a region in the image of the projected grid was recorded as a function of the rotation angle of the QWP, θ_{QWP}. The measured I values as a function of θ_{QWP} are shown in Fig. 4c. As in Fig. 3c, the measured I data and fit of the I data again follow the behavior described by the Law of Malus. However, the frequency with which the maximum in I is observed is double that shown in Fig. 3c. This result is attributed to the behavior of the QWP. When the fast axis of the QWP is oriented at $\pm 45°$ relative to the plane of polarization of the incident *lvp* light, the light is altered such that it becomes either *rcp* or *lcp*. If upon retroreflection the handedness of the circularly-polarized light is reversed, then subsequent transmission

through the same QWP in the return direction will result in the linear polarization state being orthogonal to the outgoing linear polarization state. As seen in these data, when $\theta_{QWP} = \pm 45°$, the initially *lhp* light that is transmitted by the PBS is converted to *lvp* light after passing through the QWP, reflecting off of the retroreflective background, and then passing through the QWP upon its return. This *lvp* light then passes through the secondary LP and forms an image of the Ronchi ruling on the CMOS sensor. As the QWP is rotated away from $\theta_{QWP} = \pm 45°$, the polarization state of light becomes more elliptical until its fast axis is either aligned with, or orthogonal to, the transmission axis of the primary LP. At this point, the QWP has no effect on the outgoing *lhp* light, and the returning light remains *lhp* upon retroreflection and subsequent transmission through the QWP. The *lhp* light is then fully transmitted by the PBS (rather than reflected into the camera), resulting in essentially no measurable intensity, I, at the camera. This explains why the plot of I in Fig. 4c follows the Law of Malus, but with peak I values occurring twice as frequently as in Fig. 3c. These data also verified that the 3M™ Scotchlite™ 7610 High Gain Reflective Sheeting behaves like a mirror in terms of these measured polarization properties, and was therefore a good candidate for use as a background in our instrument.

D. Projected Grid Image Quality

While the 3M™ Scotchlite™ 7610 High Gain Reflective Sheeting proved to possess the necessary polarization properties needed for the instrument, there was some concern that the sheeting would be of insufficient quality to produce high quality focused schlieren images. In this instrument, the specific concern was that the image of the projected grid element would be of insufficient quality when made incident on the original grid element as small, but finite-sized glass microspheres embedded in the material were used to achieve retroreflection. However, examination of the images from the projected grids in Figs. 3b and 4b showed that even sub-mm grid elements could be projected onto the retroreflective background and then re-imaged onto the original grid while maintaining sharp contrast between opaque and transparent regions.

E. Initial Self-Aligned Compact Focusing Schlieren System

Figure 5a shows a schematic of the component placement inside the initial compact focusing schlieren system that was constructed. Figure 5b shows an image of this system. Here, light from a 50 W white LED source (AmScope™, LED-50W) was passed through a 50-mm-diameter condenser/diffuser lens, CD (Thorlabs™, ACL5040U-DG15-A), and then through a 50.8-mm-diameter glass linear polarizer, LP[1] (Edmund Optics®, #66-183), oriented such that only *lvp* light was transmitted into a 50-mm-cubed PBS (Edmund Optics®, #65-603). This *lvp* light was then reflected onto the instrument's optical axis, providing back illumination for a $C_{cutoff} = 1$ lp/mm Ronchi ruling, RR (Data Optics, Inc.™, RR1.0-24-CG), with its lines oriented horizontally. The *lvp* light was then transmitted without refraction through a 50-mm-cube $\beta = 0.5°$ Rochon prism (RP in Fig. 5a, United Crystals™) and then through a 50.8-mm-diameter achromatic QWP (Meadowlark Optics™, AQ-200-0545-RET-ACH-L/4). An 80-200 mm, f/2.8 zoom lens (FL in Fig. 5a Nikon®, 1986) was then used to image the RR onto the 3M™ Scotchlite™ 7610 High Gain Reflective Sheeting background, RBG. A sharp image of the RR on the RBG was obtained by setting the zoom focal length of the lens to $f_{lens} = 200$ mm and then adjusting the focus ring on the lens such that the edges of the Ronchi lines appeared sharp. The RBG and end of the lens were separated by approximately 685 mm. The placement of the RR and RBG were determined using Eq. 1. An LP[2] (Thorlabs™, LPVISA100-MP2) on a rotation mount (Thorlabs™, LRM1) was fitted to a CMOS camera (Basler™, acA2040-120um) and oriented such that only *lhp* light was transmitted to the camera sensor.

A helium jet issued from a $D_{jet} = 1.65$ mm-diameter nozzle was translated along the optical axis of the instrument using a remotely-controlled 300-mm-travel translation stage (Thorlabs™, LTS300). With the nozzle initially placed approximately halfway between the RBG and lens, the image sensor was positioned to bring the nozzle into focus such that:

$$\frac{1}{f_{lens}} \approx \frac{1}{\tilde{z}_{density}} + \frac{1}{\tilde{z}_{sensor}} \tag{5}$$

where $\tilde{z}_{density}$ was the nozzle position and $\tilde{z}_{sensor}$ the camera sensor position relative to the imaging lens.

IV. Results: Initial Self-Aligned Compact Focusing Schlieren System

Figure 6 shows the first data recorded with the initial version of the self-aligned compact focusing schlieren system. For this initial test, a sequence of images was acquired with the nozzle positioned at various locations ($\pm z$, Fig. 5b) away from the focal plane of the instrument. Only time-averaged images are shown in this figure to better demonstrate the
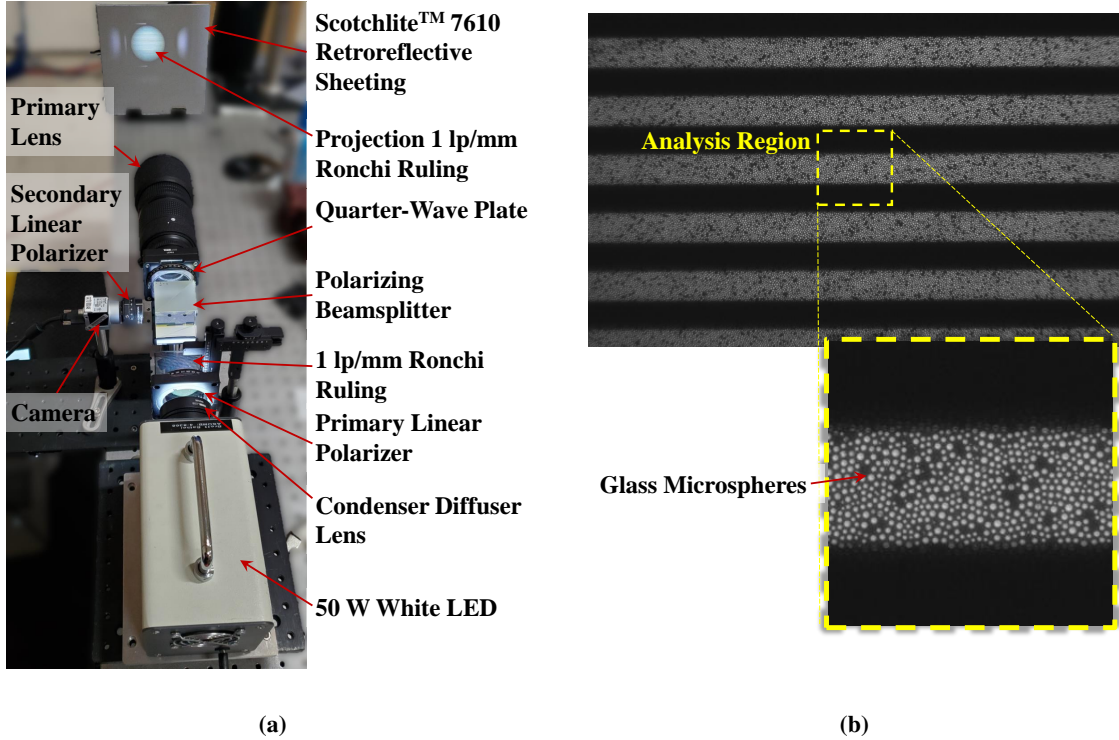
Fig. 4 **(a) Experimental setup used to characterize the ability of the retroreflective sheeting to reverse the handedness of circular polarization upon retroreflection. (b) Image of the C_{cutoff} = 1 lp/mm projected Ronchi ruling imaged by the CMOS camera. (c) Intensity, I, measurements as a function of QWP angle, θ_{QWP}.**

focusing ability of the instrument. The top row of images are the raw images from the camera while the bottom row of images are background-subtracted, meaning a background image with no flow was first subtracted from the single-shot images in order to improve image contrast. These images showed: 1) that we were able to obtain schlieren images with the instrument as light and dark regions corresponding to the jet flow structures were clearly visible and 2) that we were
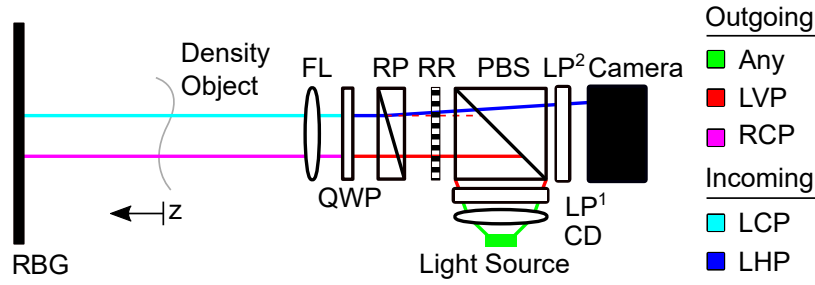
(a)
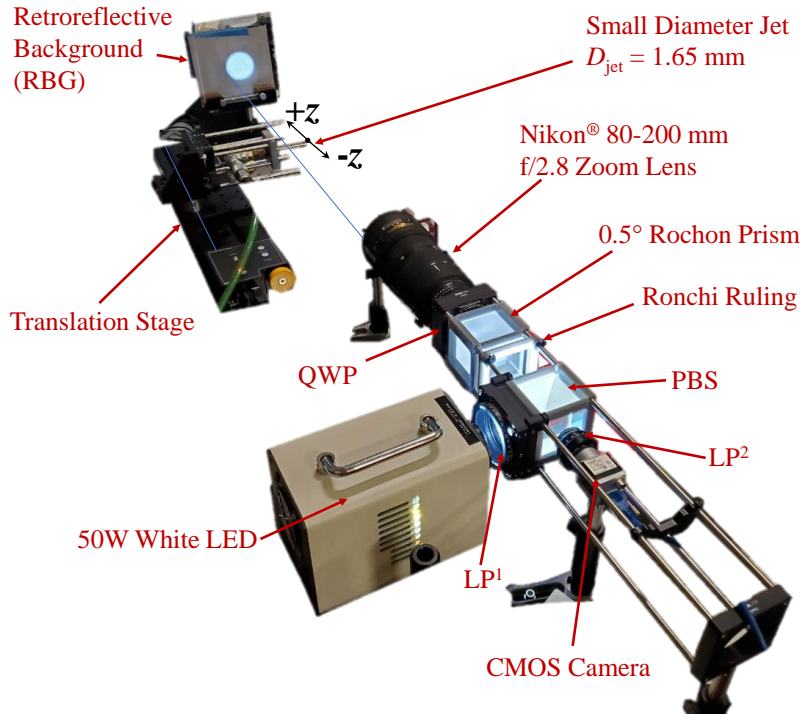
(b)

Fig. 5 **(a) Schematic of the initial self-aligned compact focusing schlieren system with the polarization states of light identified in the legend and (b) an image of the initial system assembled in the laboratory for the first demonstration test.**

able to obtain tightly focused schlieren images as the sharpness of the jet flow structures quickly decayed as the nozzle was scanned away from the focal plane of the instrument.

For a second test of the system, the small machine vision CMOS camera used to acquire the data in Fig. 6 was replaced with a LaVision™ Imager sCMOS camera. Single-shot background-subtracted images of the helium jet flow were acquired at several positions away from the focal plane of the instrument and are shown in Fig. 7a. In these single-shot images, the smaller-scale turbulent flow structures produced by the helium jet flow were clearly evident when the nozzle was positioned at the focal plane of the instrument. As the nozzle was positioned away from this focal plane, however, the sharpness of the smaller-scale structures first began to decay. As the nozzle was positioned even farther from the focal plane of the instrument, the sharpness of the larger flow structures was also reduced until the entire jet itself was barely visible ($z = \pm 50$ mm).

Next, 152.4 mm square, 6.25 mm thick clear acrylic windows were placed approximately 12.7-25.4 mm from the flow-facing side of the RBG and lens, and were oriented such that their transmitting surfaces were orthogonal to the optical axis of the instrument. Single-shot background-subtracted images of the helium flow at several nozzle positions

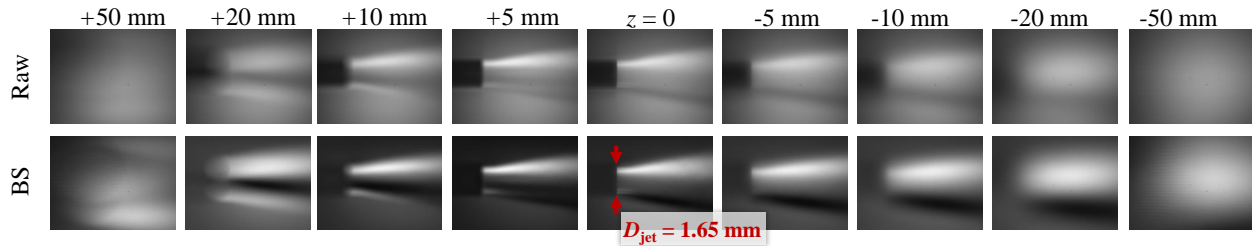| +50 mm | +20 mm | +10 mm | +5 mm | $z = 0$ | -5 mm | -10 mm | -20 mm | -50 mm |

Raw

BS

$D_{jet} = 1.65$ mm

Fig. 6 Initial (top row) raw and (bottom row) background-subtracted image data acquired with the self-aligned compact focusing schlieren system for several nozzle positions relative to the focal plane (columns).

away from the focal plane of the instrument were again acquired and are shown in Fig. 7b. The windows in this setup were intended to simulate windows that would be present in an environmental enclosure or wind tunnel test section. As can be observed in these images, when tightly-focused images are acquired with this system, the presence of the windows near the RBG or lens has little effect on the images. Only a small reduction in contrast was observed between these images and those acquired without windows in Fig. 7a, and no glare from window reflections occurred. Further details pertaining to this test can be found in Ref. [25].
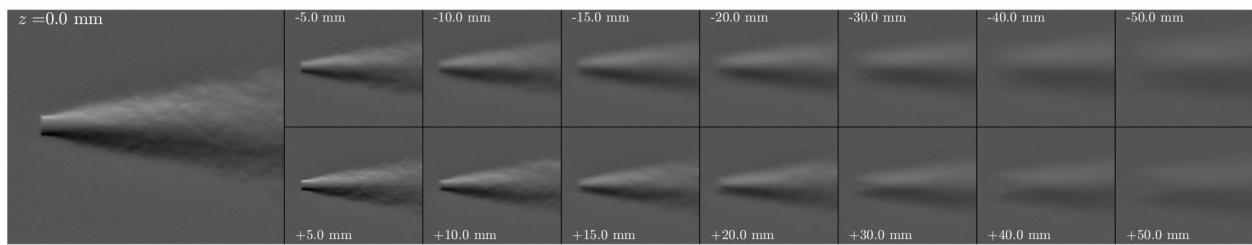
(a)
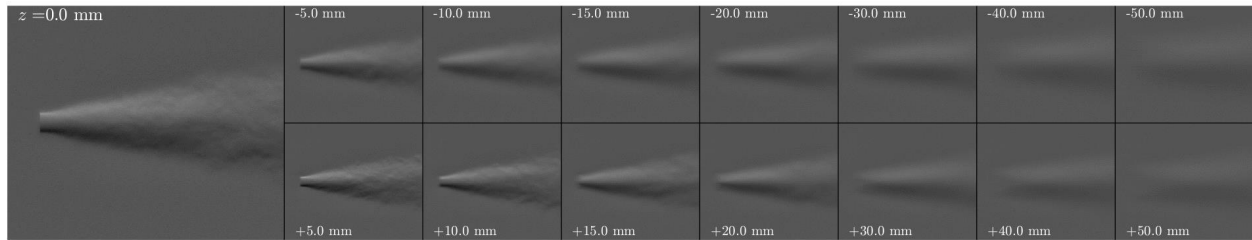
(b)

Fig. 7 Single-shot background-subtracted images of a helium jet acquired at several positions away from the instrument's focal plane (a) without and (b) with clear acrylic windows placed near the RBG and lens.

A final test with this system was performed to demonstrate its high-speed acquisition capability. For this test, a Photron™ SA-Z 2100K high-speed monochromatic camera was used to acquire the images. The white LED light source was then replaced with a Cavilux® HF laser illumination source operating at 640 nm with 50 ns pulses. The helium jet was replaced by a spark generator consisting of a pair of 4-mm-diameter electrodes that would produce breakdown in room air, generating a spherically-expanding shockwave and thermal plume. Figure 8 shows the FOV obtained with this setup. In this image, the red box corresponds to the FOV obtained when framing at 20 kHz, the green box when framing at 100 kHz, the blue box when framing at 400 kHz, and the magenta box when framing at 1 MHz. For images acquired at 1 MHz, the Cavilux™ Ultra High-Speed (UHS) module was used to drive the illumination laser.

Figure 9 shows image sequences of the resulting shockwave flow generated by the spark from the electrode pair. Note
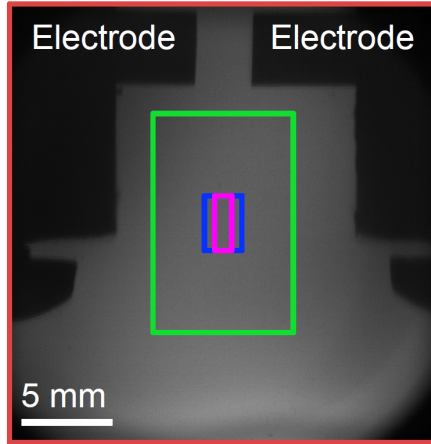
Fig. 8 Fields-of-view for laboratory visualization of a spark-generated shockwave at different framing rates. The red box corresponds to a 20 kHz imaging rate field-of-view, the green box 100 kHz, the blue box 400 kHz, and the magenta box 1 MHz.

that these are the raw images that were acquired with the camera, and no background subtraction has been performed. While acquisition at 20 kHz provided for the largest FOV, the initial shockwave generated by the spark at $t_1 + 50\ \mu s$ had left the field-of-view before the next image in the sequence was acquired. As the acquisition rate was increased, the progression of the shockwave was better captured by the system, albeit at the expense of a reduced field-of-view. These images showed that with the use of a high-speed, high-intensity pulsed illumination source, a high-speed camera, and a high-gain RBG, extremely high-speed image sequences could be obtained with the instrument.

Figure 10a shows a single-shot conventional schlieren image of a shockwave/boundary-layer interaction (SWBLI) ahead of a 76.2-mm-tall, 25.4-mm-diameter cylinder mounted on a 711.2-mm-long by 228.6-mm-wide flat plate model in the 31-Inch Mach 10 wind tunnel at NASA Langley Research Center (flow is from left to right). This image was acquired with a knife edge oriented at 45° with respect to the model surface. In this figure, the oblique shock from the leading edge of the flat plate model impinged on the cylinder near its top. Since this conventional schlieren image is path-integrated, portions of the oblique shock that did not impinge on the cylinder continue to be observed downstream and behind the cylinder. A nearly parallel (relative to the oblique shock) forward shock is observed impinging on the cylinder near its middle. An inviscid shock standing off from the forward face of the cylinder and curving around its top and proceeding downstream is also observed.

At the end of the day on the final day of this test, we were given one hour to remove the conventional schlieren hardware and set up our self-aligned compact focusing schlieren system in an attempt to obtain focused schlieren images of the SWBLI on the model. Figure 10b shows a single-shot image from the 20 kHz image sequence obtained with the system. This image was acquired from the region highlighted by the yellow box in Fig. 10a. Unfortunately, while trying to quickly set up the system, we neglected to install the QWP optic. As a result, only a bright-field image sequence (see Ref. [22] for more details) of the SWBLI with the Ronchi ruling grid lines aligned vertical to the model surface was obtained. As discussed in Sec. V.C, even without the QWP in use, the quartz/quartz Rochon prism modified the outgoing polarization state such that a bright-field image could be acquired. Note that the vertical Ronchi ruling grid line orientation used in the acquisition of Fig. 10b provided sensitivity to horizontal density gradients while almost no sensitivity to vertical density gradients was observed. Similar results were observed in conventional schlieren tests with a vertical knife edge. Close inspection of the full conventional schlieren image sequence shows that thermals outside of the wind tunnel test section as well as window scratches/chips were clearly observed, but were absent in the bright-field focused schlieren image sequence.
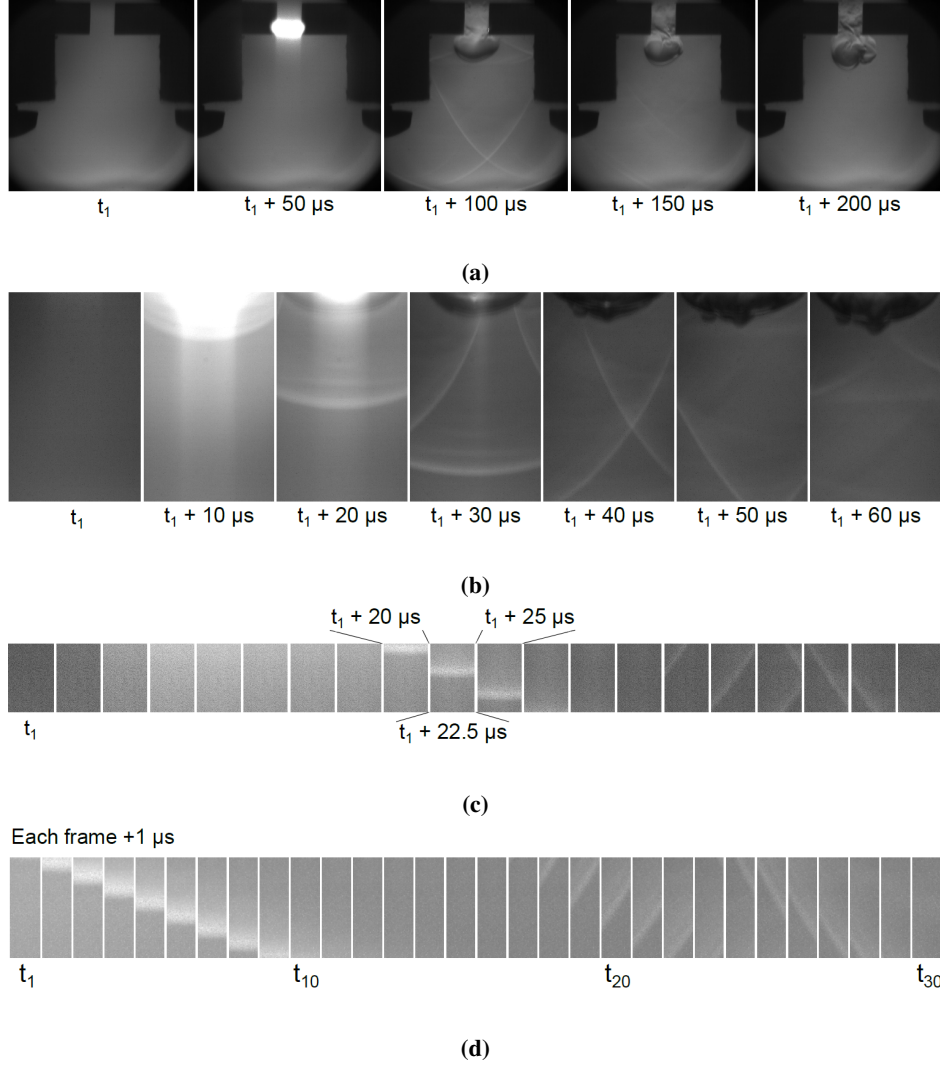
Fig. 9 **Images of the shockwave and thermal plume generated by an arc from electrodes obtained with the self-aligned compact focusing schlieren system at framing rates of (a) 20 kHz, (b) 100 kHz, (c) 400 kHz, and (d) 1 MHz.**

V. Improvements to the Initial Self-Aligned Compact Focusing Schlieren System

A. Increasing the Field-of-View: Part I

Returning to the list of qualities that were required of the system that were outlined in Sec. II, we were confident that items 1-7 could be achieved with the existing initial design. However, we had not yet been able to demonstrate item 8: develop a system where changes to the working distance and FOV could be adjusted with relative ease, and one where relatively large FOVs (> 100 mm) could be achieved, without major modification to the optical layout of the system. With the initial system, we had been able to achieve longer working distances [26] by using a longer f_{lens}, but not an easily adjustable or significantly larger FOV. The key barrier to achieving FOV adjustability as well as a significantly larger FOV was the 50-mm-cubed Rochon prism we had purchased to construct the initial system. Returning to Eq. 1, the size of the Rochon prism required that $\tilde{z}_{cutoff} \geq t_{Rochon}$. As a result, f_{lens} needed to be sufficiently long in order to project a sharp image of the grid onto the RBG placed at a distance that was of any use. With the use of a long f_{lens} lens and with $\tilde{z}_{sensor} > \tilde{z}_{cutoff}$, only a relatively small FOV could be achieved.

To achieve significantly larger FOVs, a set of thinner quartz/quartz Rochon prisms were purchased that would allow for the cutoff grid to be moved closer to the lens, thereby allowing for larger FOVs to be realized. However, with a
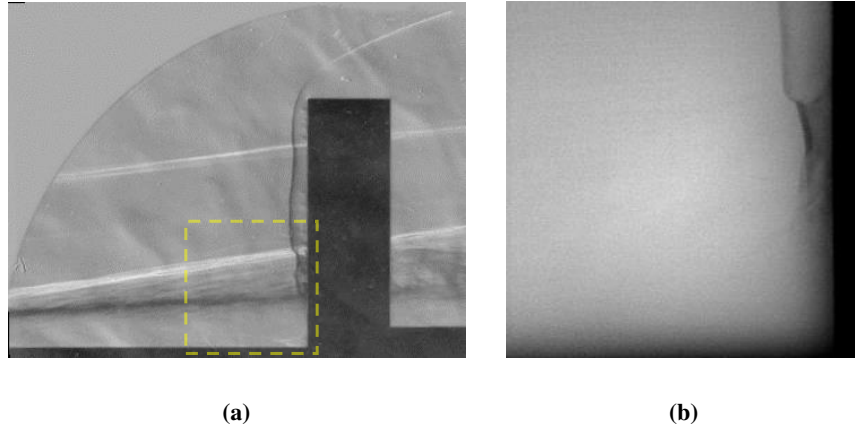
Fig. 10 **(a) Conventional schlieren and (b) bright-field focused schlieren single-shot image from 20 kHz image sequences of a shockwave/boundary-layer interaction ahead of a 76.2-mm-tall, 25.4-mm-diameter cylinder on a flat plate model in the 31-Inch Mach 10 wind tunnel.**

thinner prism comes a smaller interface angle, α (see Fig. 2), and therefore a smaller β. This then necessitated the purchase of higher frequency cutoff grids that would still allow for sensitivity adjustments according to Eq. 2. Ronchi rulings of C_{cutoff} = 0.5, 2, 5, 10, and 20 lp/mm were therefore purchased to work with these thinner Rochon prisms.

B. Eliminating Window Reflections

With the increased FOV and shorter f_{lens} lens comes an increase in the DOF. Initial testing showed that while the ability to acquire focused schlieren images remained, reflections from windows placed near the lens or RBG could be observed and diminished the instrument's signal-to-noise. One way to eliminate these reflections was to place the QWP between the window farthest from the instrument and the RBG. Unfortunately, large diameter QWPs would be prohibitively expensive to acquire. An alternative to the QWP was the use of quarter-wave film (QWF) with relatively large sizes (e.g., 500-mm by 600-mm QWF sheets from Edmund Optics®, #14-726). Several 300-mm by 300-mm QWF sheets (Edmund Optics®, #14-725) were therefore purchased and tested with the instrument. The initial tests performed without windows showed that the QWF worked as well as the QWP.

Another way to eliminate window reflections is to use an RBG material with a QWF-like property incorporated into construction of the material. Interestingly, while performing tests with several different brands of RBG materials, we discovered that some of the samples possessed this property. Further, one of the samples purchased from a local hardware supply store (Hillman™, #847336) was a prismatic retroreflective material with a honeycomb-like pattern embedded into the reflective surface. This sample performed very well in terms of providing uniform image intensity – the focusing nature of the instrument filtered out the honeycomb-like surface pattern – in addition to eliminating the need for a QWP or QWF. A planned manuscript that provides details on the performance of some of these different RBG samples is forthcoming [26].

C. Obtaining the Ideal Rochon Prism

In preparation for a follow-on test to the conventional schlieren SWBLI test in the 31-Inch Mach 10 wind tunnel (see Fig. 10a), an improved version of the self-aligned compact focusing schlieren system was set up. This setup is shown in Fig. 11a, where the optics of the system were oriented at 45° relative to the model surface so that focused schlieren images with sensitivities similar to that of the conventional schlieren system in Fig. 10a could be obtained. In this setup, a thinner quartz/quartz Rochon prism was initially used that allowed for the system to be much more compact. This, in turn, allowed for the Ronchi ruling grid to be pushed closer to the lens and enabled a larger FOV. Figure 11b shows the RBG material mounted below the bottom window of the wind tunnel with a 300-mm by 300-mm piece of QWF placed on top of the RBG. The RBG was separated by approximately 1100 mm from the end of the instrument's lens. In this figure, the projected Ronchi ruling grid lines can be observed on the RBG material (see inset), as can the shadow cast by the flat plate model. In this wind tunnel facility, optical access was such that the camera was mounted above a window

on the top wall of the facility, and the RBG and QWF materials were mounted below a window on the bottom wall of the tunnel, with the model's flat surface parallel to the side walls of the tunnel.

Initially, images acquired with this setup were of low quality as glare from window reflections significantly reduced the signal-to-noise of density gradient structures produced from a bottle of canned air. After blocking the outgoing projected light at various points between the lens and QWF material, we realized that reflections from the window closest to the lens in Fig. 11a were the source of the glare in the images. Placing a sheet of linear polarizer film between the lens and top window and rotating it a full 360° revealed that the outgoing projected light contained different polarization states.

Tests revealed that the quartz/quartz Rochon prism produced different linear polarization states in the outgoing projected light. This effect was determined to be a result of optical activity associated with the quartz material used to fabricate the Rochon prism. In the initial system, this effect induced by the quartz/quartz Rochon prism resulted in *lhp* light being returned to the PBS and passed on to the sensor unrefracted resulting in the so-call bright-field focused schlieren images. Unlike the tightly-focused image data in Fig. 10b where the quartz/quartz Rochon prism enabled this bright-field imaging without glare, the larger FOV system with the larger DOF resulted in some of the reflected light from the top window being imaged by the camera. As a result, two additional Rochon prisms were ordered from United Crystals™ that were free of optical activity effects. The first was a Rochon prism with both halves fabricated from magnesium fluoride (MgF_2) while the other was a prism fabricated with one half glass and the other half quartz as originally described by Ammann and Massey [27]. A calcite/calcite Rochon prism was also considered, but the fragility of the material meant only small prisms could be reliably fabricated. Preliminary laboratory tests with collimated light, which are detailed in a forthcoming paper [28], showed that both the MgF_2 and glass/quartz alternative Rochon prisms did not exhibit the optical activity effects that were observed with the quartz/quartz Rochon prisms.

Since the MgF_2 Rochon prism was fabricated with two halves of the same material, and therefore the outgoing light would remain strictly collinear to the instrument's optical axis, it was first installed in the system shown in Fig. 11a. However, initial tests showed that glare from reflections on the top window persisted and it was soon realized that the use of uncollimated light to back illuminate the Ronchi ruling resulted in the MgF_2 Rochon prism again inducing different polarization states in the outgoing light. It was not until the glass/quartz Rochon prism was installed in the system that reflections from the top window were truly eliminated. Figure 11c shows a focused schlieren image of a canned air jet impinging on the top surface of the flat plate model in the tunnel test section obtained with this system. In this figure, the darkened regions in the top corners in this image have been masked out as some amount of vignetting was observed in the images, a result of using a relay lens on the imaging camera. A 25.4-mm-tall bracket with a bolt hole (80/20™, 4113) can be observed in the image, and was used to adjust the focus of the instrument as well as provide a reference scale. This image showed that a moderately-sized FOV could be obtained with the system with relatively good sensitivity and DOF.

D. Increasing the Field-of-View: Part II

While the use of a thinner Rochon prism allowed for a larger FOV to be obtained relative to the system shown in Fig. 5, there was little room for adjustability of the sensitivity to density gradients as the Ronchi ruling still needed to be placed close to the lens (and therefore the Rochon prism). Ideally, if the Rochon prism could be removed then the grid element could be placed even closer to the lens and a much larger FOV could be obtained. This was not a practical solution though, as removal of the Rochon prism would then remove any ability to adjust the instrument's sensitivity. We finally realized that if we simply moved the Rochon prism in front of the lens and placed either a QWP or QWF between the Rochon prism and RBG, we could position the grid element much closer to the lens, easily adjust the sensitivity of the system, easily adjust the working distance of the system, and achieve significantly larger FOVs, all while maintaining a compact footprint. Figure 12 shows a schematic of this improved self-aligned compact focusing schlieren system.

VI. Results: Improved Self-Aligned Compact Focusing Schlieren System

Figure 13 shows images of two variants of an improved self-aligned compact focusing schlieren system. In Figs. 13a and 13b, a QWP and 1/8° (7.5 arc-minute) glass/quartz Rochon prism were placed in front of an f_{lens} = 135 mm f/2 lens (Nikon®, 1935). A C_{cutoff} = 5 lp/mm Ronchi ruling (Data Optics, Inc.™, RR5.0-24-CG) was mounted between this lens and a PBS. Light from a continuous red LED (LightSpeed Technologies™, HPLS-36DD18B) was loosely collimated and diffused by a CD lens, passed through an LP to achieve *lvp*, reflected onto the instrument's optical axis by the PBS, and used to back illuminate the Ronchi ruling. A second LP on the camera side of the PBS was oriented to pass *lhp* light. This light was then captured with an sCMOS camera (LaVision™, Imager sCMOS) with an f_{lens} = 50 mm
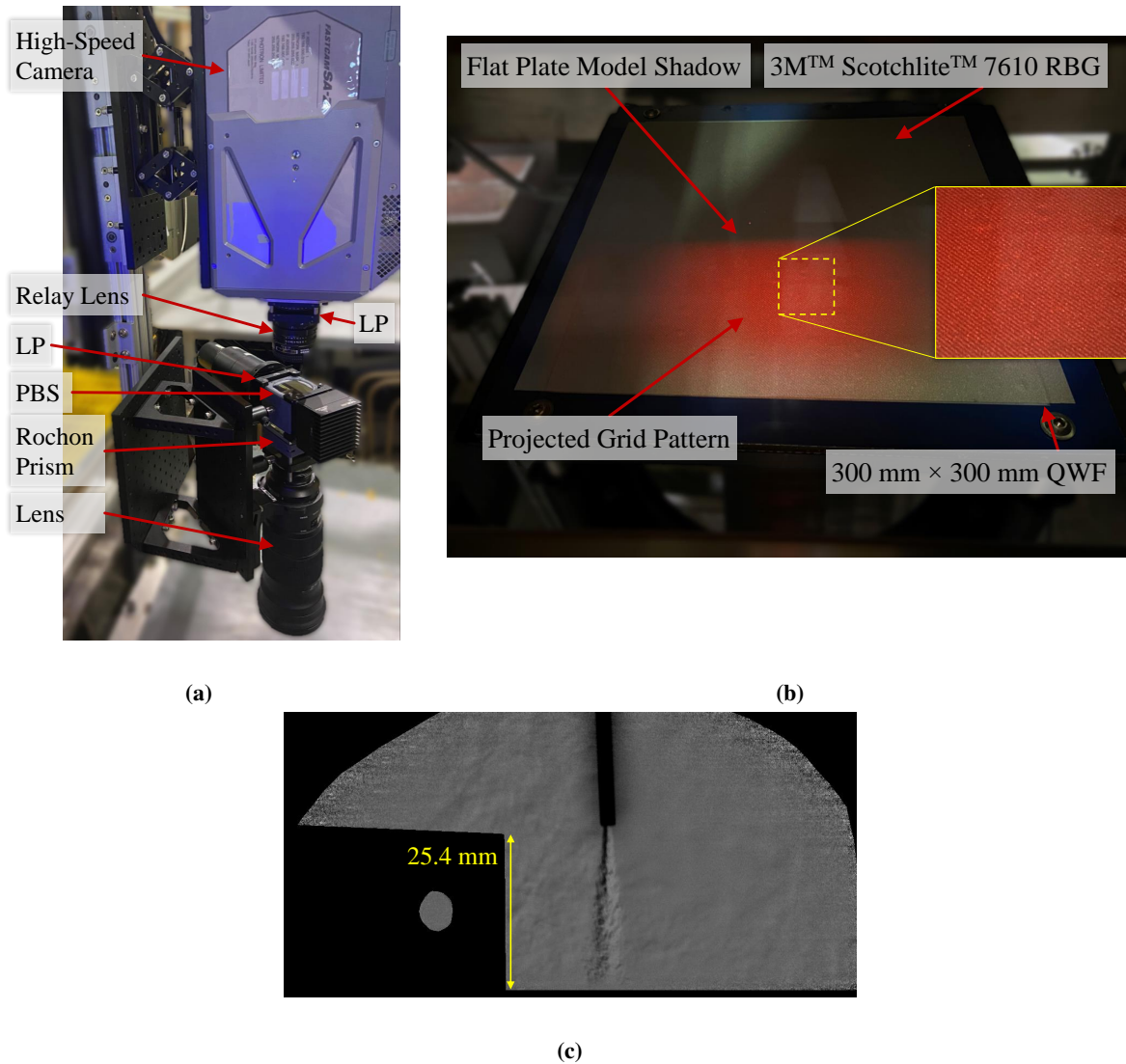
Fig. 11 High-speed compact focusing schlieren setup at 31-Inch Mach 10 wind tunnel at NASA Langley Research Center with (a) hardware above top window of tunnel and (b) RBG material with QWF below bottom window of tunnel. (c) Single-shot focused schlieren image acquired with system after switching to glass/quartz Rochon prism. RBG was placed approximately 1100 mm from the end of the lens.

f/1.4 relay lens (Nikon®, 1902). Focused schlieren images of a canned air jet from a 2-mm-diameter nozzle were acquired with the RBG first placed at approximately 2360 mm from the end of the f_{lens} = 135 mm lens. The position of the RBG was then changed such that it was approximately 1010 mm from the end of the lens. To refocus the system, the focus ring of the lens was first adjusted such that a sharp image of the Ronchi grid could be observed on the RBG. The focus ring on the f_{lens} = 50 mm lens was then adjusted such that the tip of the canned air nozzle was in sharp focus when placed approximately halfway between the RBG and the lens. Once images were acquired with this configuration, the f_{lens} = 135 mm lens was removed, and an f_{lens} = 50 mm lens (Nikon®, 1902) put in its place with the RBG at the same position (separation between the RBG and the end of the lens was 1110 mm). The system was then focused by again adjusting the focus ring on the lens so that a sharp image of the Ronchi ruling was observed on the RBG. The focus ring on the relay lens was then adjusted so that the tip of the canned air nozzle was in sharp focus when positioned approximately halfway between the lens and RBG. The exposure on the camera was set to 2.5 ms. For each test, less
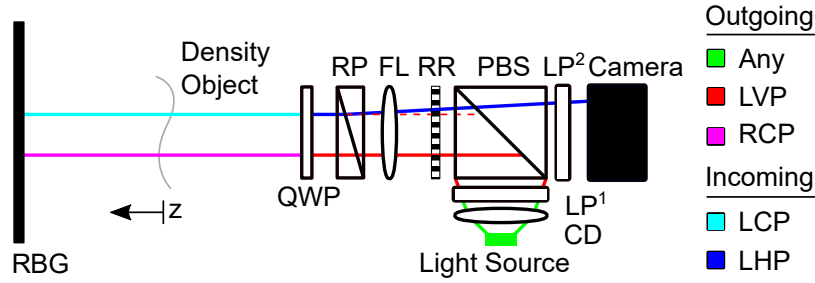
Fig. 12 Schematic of improved self-aligned compact focusing schlieren system. Note that a QWP can be replaced by QWF and may be positioned anywhere between the RBG and Rochon prism, RP.

than one minute was needed to bring the unfocused system into focus.
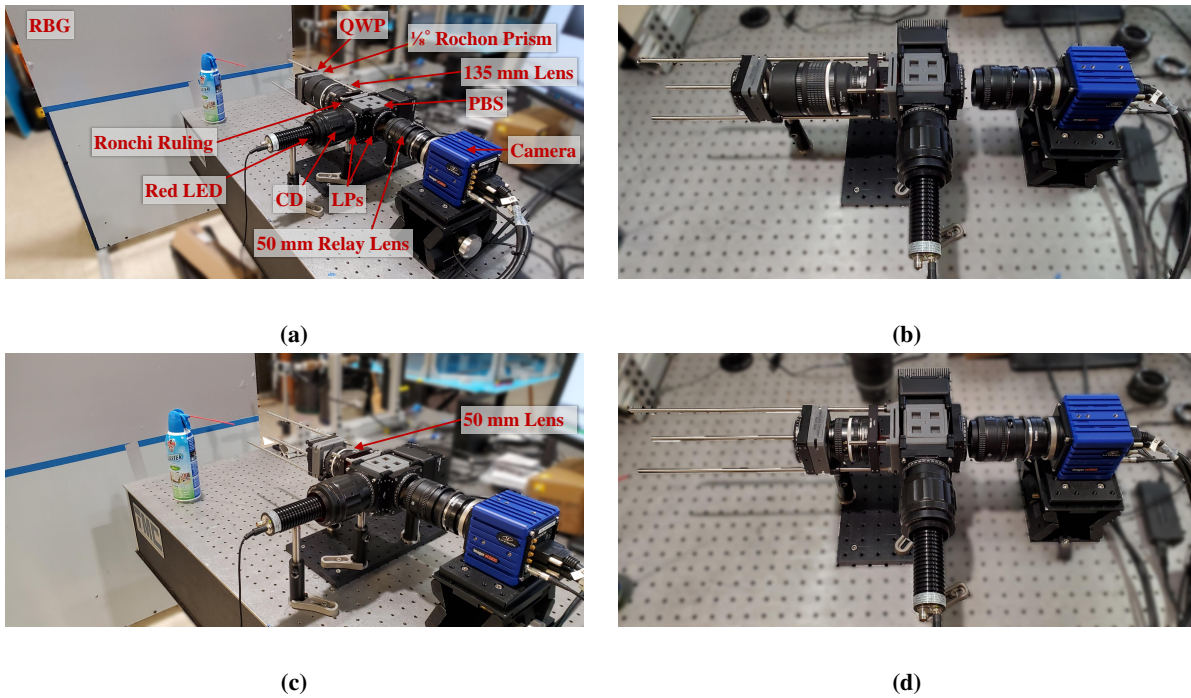

(a)

(b)

(c)

(d)

Fig. 13 Images of improved self-aligned compact focusing schlieren system. (a) Perspective and (b) top views of system with 135 mm lens. (b) Perspective and (d) top views of system with 50 mm lens.

Figures 14a and 14b show single-shot focused schlieren images of the canned air jet using the f_{lens} = 135 mm lens setup (Figs. 13a and 13b) with the RBG placed 2360 mm and 1010 mm from the end of the lens, respectively. The jet was placed approximately halfway between the RBG and the end of the lens. These images demonstrate that a single self-aligned compact focusing schlieren system can be quickly adjusted to accommodate different working distances in a test environment or achieve different FOVs if the working distance can be changed. Figure 14c shows a single-shot focused schlieren image of the canned air jet acquired with the f_{lens} = 50 mm lens setup (Figs. 13c and 13d) with the RBG placed 1110 mm from the end of the lens. Again, the jet was placed halfway between the RBG and the end of the lens in this image. The black masked-out diagonal features in the image correspond to the 6-mm-diameter cage rods used to mount the optics and maintain their alignment (these are most clearly shown in Fig. 13d on the left-hand-side of the instrument). This image demonstrates that a relatively large FOV can be obtained with the improved self-aligned compact focusing schlieren system using a short f_{lens} lens.

These figures highlight other benefits of this system: commercially-available camera lenses can be used with the system, and the use of such lenses further simplifies the focus adjustment of the system. Also, as an alternative to

switching between the fixed f_{lens} = 135 mm and f_{lens} = 50 mm lenses to obtain two different FOVs, a zoom camera lens could also have been implemented. This would allow for even faster adjustment of the working distance and FOV. The use of a high-intensity, pulsed light source would also have improved the visibility of the small scale turbulent structures farther from the tip of the nozzle, as the use of a continuous LED light source and 2.5 ms camera exposure resulted in some blurring of these structures.
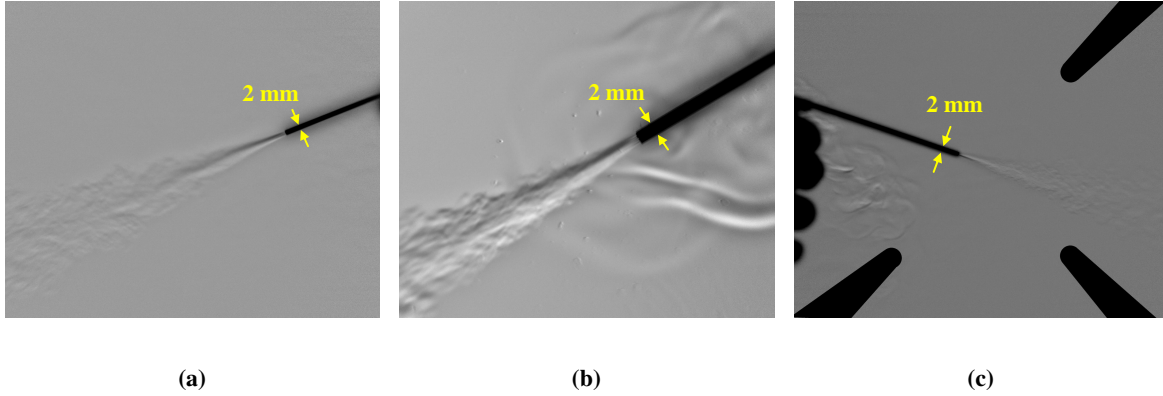

Fig. 14 Single-shot images obtained with improved self-aligned compact focusing schlieren system with (a) RBG placed approximately 2360 mm from end of 135 mm lens, (b) RBG placed approximately 1010 mm from end of 135 mm lens, and (c) RBG placed approximately 1110 mm from end of 50 mm lens. Canned air jet was positioned approximately halfway between RBG and the end of the lens in all figures.

Figure 15 shows images of another version of the improved self-aligned compact focusing schlieren system that was used to visualize a helium plume from a 60° nozzle (McMaster-Carr®, 32885K143) interacting with a bed of 254 μm silicon carbide particles (McMaster-Carr®, 4780A36) during a PSI event. In Fig. 15a, the 1/8° glass/quartz Rochon prism was placed in front of an f_{lens} = 300 mm f/2.8 lens (Nikon®, 2186). Pulsed 640 nm light from the Cavilux™ HF laser was loosely collimated and diffused by a CD lens, passed through an LP to achieve *lvp*, reflected onto the instrument's optical axis by the PBS, and used to back illuminate a C_{cutoff} = 1 lp/mm Ronchi ruling. Images were acquired at 20 kHz with a 40 ns pulse width. A Photron™ SA-Z 2100K high-speed camera with an LP mounted in front of the sensor was used to image the PSI event. Figure 15b shows a perspective view of this setup with the PSI test chamber and a piece of 300-mm by 300-mm QWF covering the RBG behind the test chamber. The test chamber was essentially a closed box with large acrylic windows used to contain the particles while allowing for visualization of the PSI event.
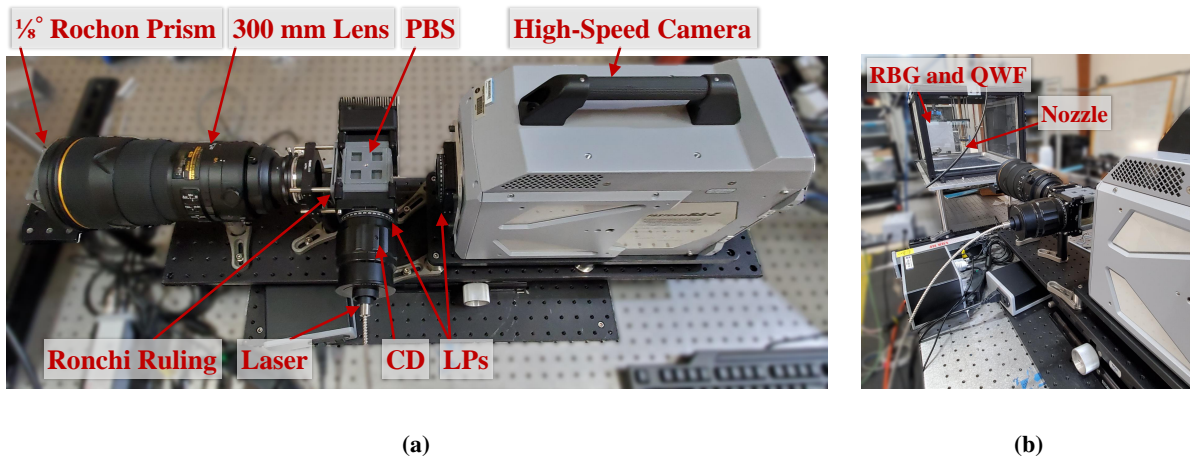

Fig. 15 Images of (a) top and (b) perspective views of improved self-aligned compact focusing schlieren system for PSI flow and particle imaging with 300 mm lens.

Figure 16 shows single-shot images from a 20 kHz image sequence of a PSI event. In Fig. 16a, the faint signature of the helium plume is visible on the left-hand-side of the image before it has impinged on the particle bed. In Fig. 16b, particles can be observed that have been displaced from the top of the particle bed. In this image, the faint signature of the helium plume is still observed towards the left-hand-side of the image while particles towards the right-hand-side of the image can be observed with sharp focus as they travel in the focal plane of the instrument and away from the plume. The particles towards the left-hand-side of the image are traveling away from the focal plane and therefore do not appear as sharply in-focus. In Fig. 16c, the signature of the helium plume becomes stronger towards the left-hand-side of the image. In-focus particles are still observed on the far right-hand-side of the image as they continue to travel outward from the helium plume. However, the majority of the particles in the FOV are traveling away from the focal plane of the instrument and therefore appear significantly out-of-focus. In Fig. 16d, while the signature of the helium plume can still be observed, nearly all of the particles are now out of focus as the crater beneath the plume expands and most particles in the FOV are traveling away from the instrument's focal plane. It should be noted that for all of these figures, the small clear aperture of the 1/8° glass/quartz Rochon prism visibly limited the amount of light collected by the instrument when placed at the end of the f_{lens} = 300 mm lens and may also have increased the DOF of the system. Larger glass/quartz Rochon prisms are currently on order and will be incorporated into this setup to eliminate these issues.

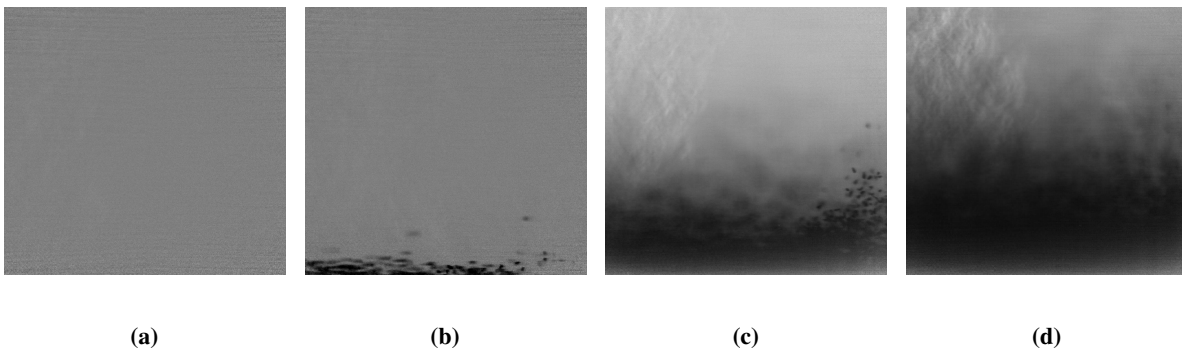(a)   (b)   (c)   (d)

Fig. 16 Single-shot images from a 20 kHz image sequence obtained with improved self-aligned compact focusing schlieren system with when (a) weak schlieren signature from helium plume becomes visible, (b) particles first become visible, (c) particles away from focal plane are out of focus, and (d) signature of plume is clearly visible and most particles are out of focus.

VII. Conclusions

This paper discusses the development of a self-aligned compact focusing schlieren system that can be used to visualize density gradients and other features (e.g., particles) in a flow within a narrow depth-of-field. Unlike existing focusing schlieren systems, this system makes use of only a single grid element, with an image of the grid being projected onto a retroreflective background, and then that projection being reimaged back onto the original grid element. This results in the system being self-aligned. The use of several specific optical elements to act on the polarization state of the light provides adjustment of sensitivity to density gradients present in the object plane. The system can also be arranged to take advantage of the polarization state of light so that reflections from windows in ground test facilities can be eliminated. This allows for focusing schlieren visualizations to be acquired at normal incidence to these windows. Since all of the optical elements used to construct the system can be placed within a relatively small footprint, the resulting focusing schlieren system is very compact and can be mounted to, or placed directly in front of, a camera with relative ease. Tests with the system showed that both short and long working distances as well as different fields-of-view could be achieved quickly (within minutes) and with little modification to the system. The use of commercially-available camera lenses further simplifies the adjustment of the working distance and field-of-view of the system. Since the system projects an image of the grid element onto a retroreflective background and then reimages the grid with the same optics, it only requires single-sided optical access to the measurement volume. While an original goal in the development of this system was to visualize plume/surface interaction events, the focusing ability, quality of the schlieren images, image acquisition rates that can be achieved, and relative ease and quickness with which the instrument can be set up makes it attractive for use in ground test facilities where the use of a path-integrated

conventional schlieren system would limit data quality.

Acknowledgments

Disclosures

In this work, specific vendor and manufacturer names are explicitly mentioned only to accurately describe the test hardware. The use of vendor and manufacturer names does not imply endorsement by the U.S. Government. Patents pending for the technology described in this work.

References

[1] Krehl, P., and Engemann, S., "August Toepler — The first who visualized shock waves," *Shock Waves*, Vol. 5, No. 1-2, 1995, pp. 1–18. https://doi.org/10.1007/bf02425031.

[2] Settles, G. S., *Schlieren and Shadowgraph Techniques*, Springer Berlin Heidelberg, 2001. https://doi.org/10.1007/978-3-642-56640-0.

[3] Settles, G. S., and Hargather, M. J., "A review of recent developments in schlieren and shadowgraph techniques," Vol. 28, No. 4, 2017, p. 042001. https://doi.org/10.1088/1361-6501/aa5748.

[4] Hartmann, J., "Den akustiske Luftstraalegenerator," *Fysysk Tidss*, 1940, pp. 65–113.

[5] Hartmann, J., "The Acoustic Air-Jet Generator," Technical Translation TT–20210016495, National Aeronautics and Space Administration, Nov. 2021. Originally published in 1940. Translation by J.M. Weisberger.

[6] Schardin, H., "Die Schlierenverfahren und ihre Anwendungen," Springer Berlin Heidelberg, 1942, pp. 303–439. https://doi.org/10.1007/bfb0111981.

[7] Burton, R. A., "A Modified Schlieren Apparatus for Large Areas of Field," Vol. 39, No. 11, 1949, p. 907. https://doi.org/10.1364/josa.39.000907.

[8] Weinstein, L. M., "An Improved Large-Field Focusing Schlieren System," *29th AIAA Aerospace Sciences Meeting*, 1991. https://doi.org/10.2514/6.1991-567, AIAA Paper 1991-567.

[9] Weinstein, L. M., "Large-Field High-Brightness Focusing Schlieren System," *AIAA Journal*, Vol. 31, No. 7, 1993, pp. 1250–1255. https://doi.org/10.2514/3.11760.

[10] Boedeker, L. R., "Analysis and construction of a sharp focussing schlieren system," Ph.D. thesis, Massachusetts Institute of Technology, 1959.

[11] Gartenberg, E., Weinstein, L. M., and Lee, E. E., "Aerodynamic Investigation with Focusing Schlieren in a Cryogenic Wind Tunnel," *AIAA Journal*, Vol. 32, No. 6, 1994, pp. 1242–1249. https://doi.org/10.2514/3.12126.

[12] Whalen, T. J., Kennedy, R. E., Laurence, S. J., Sullivan, B., Bodony, D. J., and Buck, G., "Unsteady Surface and Flowfield Measurements in Ramp-Induced Turbulent and Transitional Shock-Wave Boundary-Layer Interactions at Mach 6," *AIAA Scitech 2019 Forum*, 2019. https://doi.org/10.2514/6.2019-1127, AIAA Paper 2019-1127.

[13] Heineck, J. T., "Retroreflection Focusing Schlieren System," , May 1996. US Patent 5,515,158.

[14] Weinstein, L. M., "Review and update of lens and grid schlieren and motion camera schlieren," *The European Physical Journal Special Topics*, Vol. 182, No. 1, 2010, pp. 65–95. https://doi.org/10.1140/epjst/e2010-01226-y.

[15] Fagan, A. F., L'Esperance, D., and Zaman, K. B., "Application of a Novel Projection Focusing Schlieren System in NASA Test Facilities," *AIAA Aviation Forum*, 2014. https://doi.org/10.2514/6.2014-2522, AIAA Paper 2014-2522.

[16] Buckner, B. D., Trolinger, J. D., and L'Esperance, D., "Digital focusing schlieren imaging," *SPIE Optical Engineering + Applications*, 2015. https://doi.org/10.1117/12.2189533.

[17] Schoegl, I., Pisano, A. J., and Sedky, G., "Development of a Compact Focusing Color Schlieren Technique," American Institute of Aeronautics and Astronautics, 2016. https://doi.org/10.2514/6.2016-1765, AIAA Paper 2016-1765.

[18] L'Esperance, D., and Buckner, B. D., "Focusing schlieren systems using digitally projected grids," *SPIE Optical Engineering + Applications*, 2017. https://doi.org/10.1117/12.2274079, paper 10373-26.

[19] Buckner, B. D., and L'Esperance, D., "Schlieren unwrapped: distortion correction in digital focusing schlieren," *SPIE Optical Engineering + Applications*, 2019. https://doi.org/10.1117/12.2528081, paper 11102-26.

[20] MetroLaser®, Inc., "High-Speed Schlieren," Online, Nov. 2021. Website: http://www.metrolaserinc.com/technologies/high-speed-schlieren/. Accessed Nov 9th, 2021.

[21] Weisberger, J., Bathel, B. F., Jones, S. B., and Herring, G. C., "Focused Laser Differential Interferometry Measurements at NASA Langley 20-Inch Mach 6," American Institute of Aeronautics and Astronautics, 2019. https://doi.org/10.2514/6.2019-2903, AIAA Paper 2019-2903.

[22] Bathel, B. F., Weisberger, J. M., Herring, G. C., King, R. A., Jones, S. B., Kennedy, R. E., and Laurence, S. J., "Two-point, parallel-beam focused laser differential interferometry with a Nomarski prism," Vol. 59, No. 2, 2020, pp. 244–252. https://doi.org/10.1364/ao.59.000244.

[23] Onuki, K., Nakajima, M., Okamoto, T., Kawagishi, N., and Yamamoto, H., "Brightness improvement by polarization modulation in the aerial imaging by retro-reflection (AIRR)," *Imaging and Applied Optics 2016*, OSA, 2016. https://doi.org/10.1364/3d.2016.jt3a.65, Paper JT3A.65.

[24] Jenkins, F., *Fundamentals of Optics*, 4th ed., McGraw-Hill, New York, 1976. Pp. 503–504.

[25] Bathel, B., and Weisberger, J., "Compact, self-aligned focusing schlieren system," *Optics Letters*, 2021, pp. 3228–3331. https://doi.org/10.1364/ol.428011.

[26] Weisberger, J. M., and Bathel, B. F., "Single Source/Cutoff Grid, Self-Aligned Focusing Schlieren System," 2021. Forthcoming publication.

[27] Ammann, E. O., and Massey, G. A., "Modified Forms for Glan–Thompson and Rochon Prisms," *Journal of The Optical Society of America*, Vol. 58, No. 11, 1968, pp. 1427–1433. https://doi.org/10.1364/josa.58.001427.

[28] Weisberger, J. M., and Bathel, B. F., "Characterization of Rochon Prisms for Bi-Directional Imaging Applications," 2021. Forthcoming publication.